Analysis of internal stress build-up during deposition of nanocrystalline Ni thin films using transmission electron microscopy

Gunnar Lumbeeck[1], Adeline Delvaux[2], Hosni Idrissi[2,1], Joris Proost[2], Dominique Schryvers[1].

[1]Electron Microscopy for Materials Science (EMAT), Department of Physics, University of Antwerp, Groenenborgerlaan 171, B-2020 Antwerp, Belgium
[2]Institute of Mechanics, Materials and Civil Engineering, UCLouvain, Place Sainte Barbe 2, B-1348 Louvain-la-Neuve, Belgium

Abstract

Ni thin films sputter-deposited at room temperature with varying Ar pressures were investigated with automated crystal orientation mapping in a transmission electron microscope to uncover the mechanisms controlling the internal stress build-up recorded in-situ during deposition. Large grains were found to induce behaviour similar to a stress-free nucleation layer. The measurements of grain size in most of the Ni thin films are in agreement with the island coalescence model. Low internal stress was observed at low Ar pressure and was explained by the presence of large grains. Relaxation of high internal stress was also noticed at the highest Ar pressure, which was attributed to a decrease of Σ3 twin boundary density due to a low deposition rate. The results provide insightful information to better understand the relationship between structural boundaries and the evolution of internal stress upon deposition of thin films.

Keywords: thin films, nickel, electron microscopy, internal stress, grain boundaries

1. Introduction

In the past, mechanical properties of nickel (Ni) thin films such as hydrogen-induced effects [1,2], the shift in deformation mechanisms in the Hall-Petch transition region [3] and internal stress induced during deposition [4] have been heavily investigated. The latter has been a matter of attention for close to 70 years now [4] and several mechanisms explaining the stress build-up during deposition have been suggested. Some parameters are still under heavy debate such as the role of adatoms on the strain field [5], excess vacancy (or interstitial) reduction [6,7] and the influence of dislocations [8]. On the other hand, some mechanisms are well-established like lattice mismatch, capillarity stress [9], or as will be applied in this work, the island coalescence model [10]. By approximation, the exterior of growing grains can be considered as rounded surfaces. During contact with adjacent islands, the system can lower its net free energy by reducing the high surface energy and by creating an interface with a relatively low interfacial energy [11]. This interface will take on the physical characteristics of an elastic crack. During the closing of this crack (this mechanism is commonly referred to as 'zipping'), the islands involved become elastically strained, contributing to the internal stress measurement. Furthermore, it is assumed that the zipping mechanism occurs on a relatively short time in comparison to the required time needed for the islands' elastic relaxation to

occur [11], thus inducing a permanent residual strain in the film. If the film would be deposited uniformly, no internal stress would build up since the film can grow in an energetically favourable condition, leading to a single-crystal structure. It can occur that even though the initial deposition starts uniformly, islands can still start to form from a certain thickness; the uniform layer is referred to as a nucleation layer.

On top of the uncertainty on the nucleation mechanism(s), another interesting aspect is the resulting texture and grain size in thin films as it strongly influences the mechanical behaviour of the material. For example, the Hall-Petch curve is depending on the combined contribution of the orientation texture and grain boundary distribution [12]. X-ray diffraction (XRD) [13] and electron backscatter diffraction (EBSD) are typically used for the examination of these characteristics, although the first method does not provide local information and the latter is limited to microscaled samples [12]. For nanoscaled films, in which the thickness usually does not exceed ~100 nm, more advanced transmission electron microscopy (TEM) techniques are required. In this research, nanocrystalline Ni thin films were sputter-deposited on a Si substrate during which the stress was measured in-situ. The stress-thickness behaviour observed during deposition is explained using microstructural information extracted from automatic crystallographic orientation mapping in TEM (ACOM-TEM) [14–16]. The results provide information on the relationship between structural boundaries and the internal stress evolution in nanocrystalline Ni thin films. Similar results can be achieved using transmission kikuchi diffraction (TKD) as shown by Kacher *et al*.[17,18] who used this technique to display the formation of twin boundaries in annealed nanocrystalline Ni thin films. They were able to prove through TKD the importance of the formed boundaries for the equilibrium state of their samples and were able to resolve features as small as 5 nm twins. The most suited transmission orientation mapping technique depends on the requirements of the sample; TKD yields a higher angular resolution due to the presence of the kikuchi lines while ACOM-TEM is more fitting for beam-sensitive samples [19].
Knowledge on the microstructure can be useful to explain results observed at the macroscale. For example, the discussed Ni thin films were also part of the work performed by Delvaux *et al*. [20] who studied the hydriding behaviour of these films through water electrolysis, showing a connection between the solubility of hydrogen and the film's average grain size.

2. Experimental details

A double-sided polished, 380 µm thick silicon (Si) substrate was coated with a 5 nm amorphous TiO_2 layer, which was sputter-deposited at a rate of 0.3 nm/min in an Orion 5 multi-target sputtering chamber from AJA International. The thin amorphous TiO_2 coating (shown in Figure S1 of the supplementary info) acts as a passivation layer to protect the Si from oxidation and to ensure the adhesion of the Ni layer. On top of this TiO_2 layer, nanocrystalline Ni thin films were magnetron sputter-deposited from a pure Ni target (K.J. Lester Co.) at room temperature with an argon (Ar) plasma pressure ranging between 0.27 Pa and 1.07 Pa until a thickness of 100-120 nm was reached. The amount of scattering is proportional with the Ar pressure, thus the deposition rate and time were proportionally decreased and increased respectively to compensate for this effect; detailed values are provided in

Pressure (Pa)	Deposition rate (nm/min)	Deposition time (min)

0.27	2.0	50
0.40	1.7	60
0.53	1.5	65
0.67	1.3	75
1.07	1.1	95

Table **1**. Measurement of the final thickness was performed with Inductively Coupled Plasma – Optical Emission Spectrometry (Agilent Technologies 5100 ICP-OES); more details are provided by Delvaux *et al*. [20].

Pressure (Pa)	Deposition rate (nm/min)	Deposition time (min)
0.27	2.0	50
0.40	1.7	60
0.53	1.5	65
0.67	1.3	75
1.07	1.1	95

Table 1: Deposition rate and deposition time used at each Ar pressure.

The internal stress was measured in-situ using a high-resolution curvature measurement setup aimed at the substrate in the deposition chamber [17]. Using multiple laser beams directed towards the deposited film, the curvature of the film can be quantified based on the position of the reflected beams [22]. Cross-sectional TEM samples were prepared from films deposited under different conditions with a focused ion beam (FIB) using the "lift-out" procedure (more details can be found in the supplementary information). To improve the reliability of the ACOM-TEM results, careful thinning was performed with FIB to minimize the amount of overlapping grains.

A Tecnai G2 microscope (FEG, 200 kV) from Thermofisher Scientific equipped with the ASTAR system from Nanomegas was used to perform high resolution TEM (HR-TEM) and ACOM-TEM [23]. Using electron precession with an angle of 0.4°, the dynamical scattering effects were minimized which will facilitate the automatic indexation of the diffraction patterns during post-treatment [24]; the resulting electron probe size was ~2 nm. Using the software package from Nanomegas, pre-calculated electron diffraction patterns were generated and cross-correlated to every obtained pattern [23]. The orientation resolution of this database was 0.5°. Once all patterns are indexed, further processing is performed with the Orientation Imaging Microscopy analysis software from EDAX Inc. This includes noise reduction, statistical analysis and interface mapping. Non-indexed and mis-indexed points were corrected using a clean-up method commonly used on electron backscatter data [25].

3. Results and Discussions

The stress-thickness data displaying the internal stress build-up are shown in Figure 1a. Every curve can be divided in three sequential characteristic sections. Firstly, the stress remains stable at a constant value, which could be explained by the formation of a single crystal nucleation layer without or with just a few grain boundaries (GBs) or an amorphous structure. For the Ni thin film prepared at 0.27 Pa, we observed that the stress remained almost zero

during the entire deposition. All other samples show a sudden increase, indicating typically the end of the nucleation layer [26] and the start of the formation of GBs. For 0.40 Pa and 0.53 Pa, the expected nucleation layer thickness is respectively 50 nm and 30 nm, as measured from the stress-thickness data in Figure 1a. For the samples deposited with 0.67 Pa and 1.07 Pa, the nucleation layer ends at around 10 nm.

Secondly, the initial increasing slope can be used as an indication for the grain size based on the 'zipping mechanism' as suggested by Nix and Clemens [10], where the tensile stress increase is inversely proportional to the grain size. It needs to be restated here that every Ni film was deposited at a different deposition rate, which can be proportional to the tensile stress as was proven by Hearne *et al*. [27] and Kongstein *et al*. [28] for electrodepositing Ni or Cu, respectively. However, since each film also had an Ar pressure in the deposition chamber inversely proportional to the used deposition rate, comparable deposition conditions are induced in all samples. Aside from 0.27 Pa, all samples show a similar slope, thus the grain size is expected to be similar. At any point on the curve, the stress contributed by the incremental layer of film deposited can be quantified by taking the derivative at that thickness [29]; an incremental internal stress of ~1.1 GPa was estimated from the initial slope. Finally, for the samples prepared at the highest Ar pressures, 0.67 Pa and 1.07 Pa, a downward bending of the curve is seen. This effect together with all predictions described in this section will be cross-correlated with the TEM results. To improve readability, the colour labelling applied in Figure 1a will also be used in the succeeding figures.

Representative ACOM-TEM maps of the different samples are shown in Figure 1b. Several ACOM-TEM maps were recorded per sample to improve statistical analysis and yielding a total of 99 grains for the sample prepared at 0.27 Pa and between 400 and 1000 grains for the other samples. The deposition direction is horizontal in each map, growing from left to right (i.e., the Si/TiO_2 substrate is for every map on the left hand side, out of the frame). An example of a high resolution TEM (HR-TEM) image showing the Si/TiO2/Ni interface is provided in the supplementary information.

The viewing direction in these figures is the normal direction (ND) to the FIB sample. The used reference system with ND, rolling direction (RD) and transverse direction (TD) is shown in Figure 1b. Starting from the 0.27 Pa sample, we can observe that the thin film mostly consists of large grains spanning the entire deposition width with only a few high angle GBs (HAGBs), which are represented in the maps as black lines and include possible twin boundaries. This is in agreement with the conclusion obtained from Figure 1a. For the 0.40 Pa and 0.53 Pa samples, a respective nucleation layer of 50 nm and 30 nm was anticipated from the observations made in Figure 1a. Instead of the expected single-crystal nucleation layer, several large grains originating on the TiO_2 side are observed in these films. It has already been shown in the literature that an inverse correlation exists between grain size and internal stress in electrodeposited Ni thin films [12,30]. Aside from the uniformly distributed films (0.67 and 1.07 Pa), the largest grains in these examined films mostly agglomerate on the TiO_2 side, explaining the delay in stress build-up during deposition.

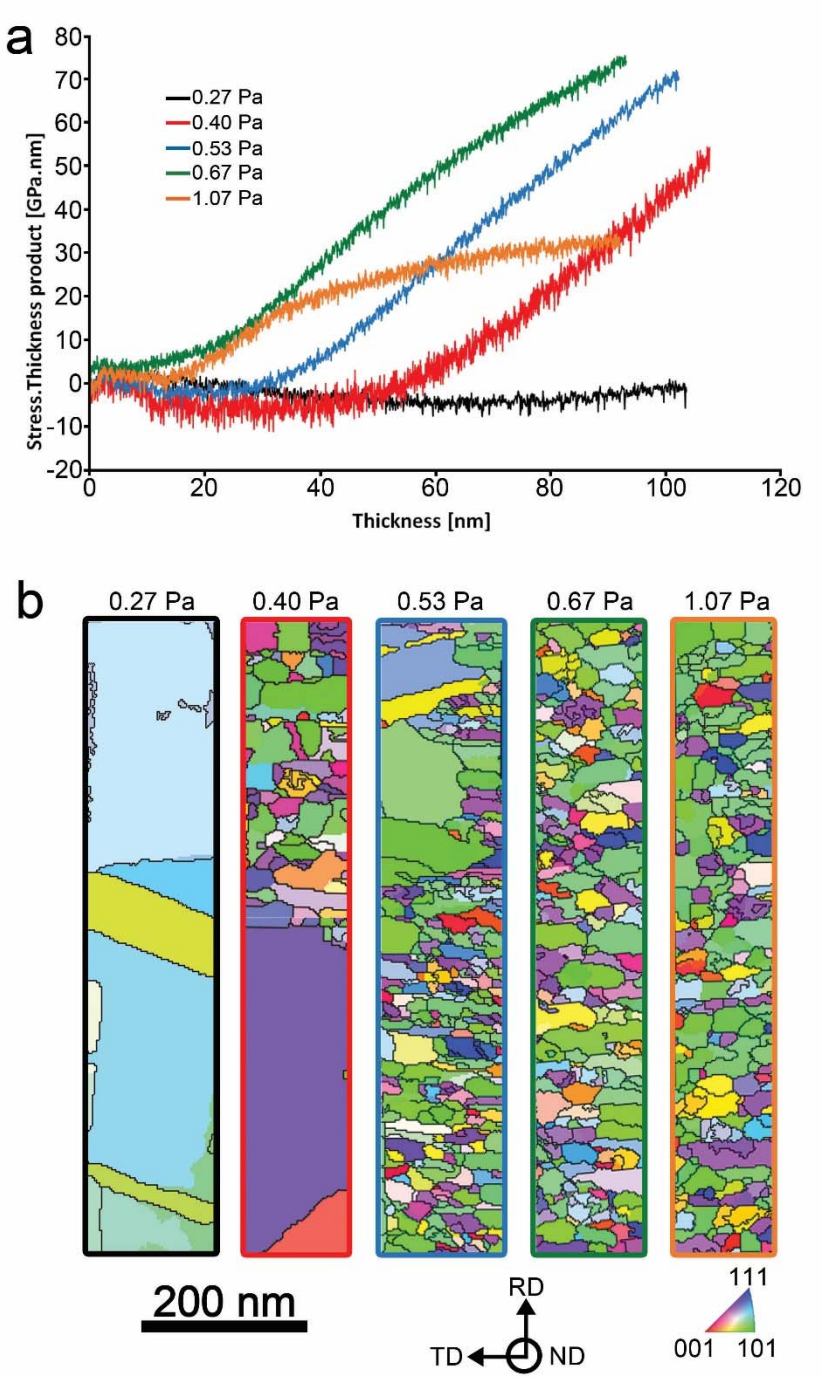

Figure 1: (a) Stress-thickness curves showing the stress build-up in the Ni thin film deposited at different Ar pressures. (b) ACOM-TEM maps of Ni thin films deposited with varying Ar pressure, viewed normal to the FIB sample. Showing from left to right: 0.27 Pa (black contour), 0.40 Pa (red), 0.53 Pa (blue), 0.67 Pa (green) and 1.07 Pa (orange). The indexation colour scaling is included as inset figure. The grains are separated by black lines representing HAGBs. The reference system is provided at the bottom.

A detailed grain size distribution is provided in Figure 2, showing that the average grain size and spread decreases with increasing Ar pressure. Table 2 displays the average grain size derived from Figure 2. The mean stress per film is also provided in Table 2, extracted from Figure 1a by dividing the final stress.thickness value by the total film thickness.

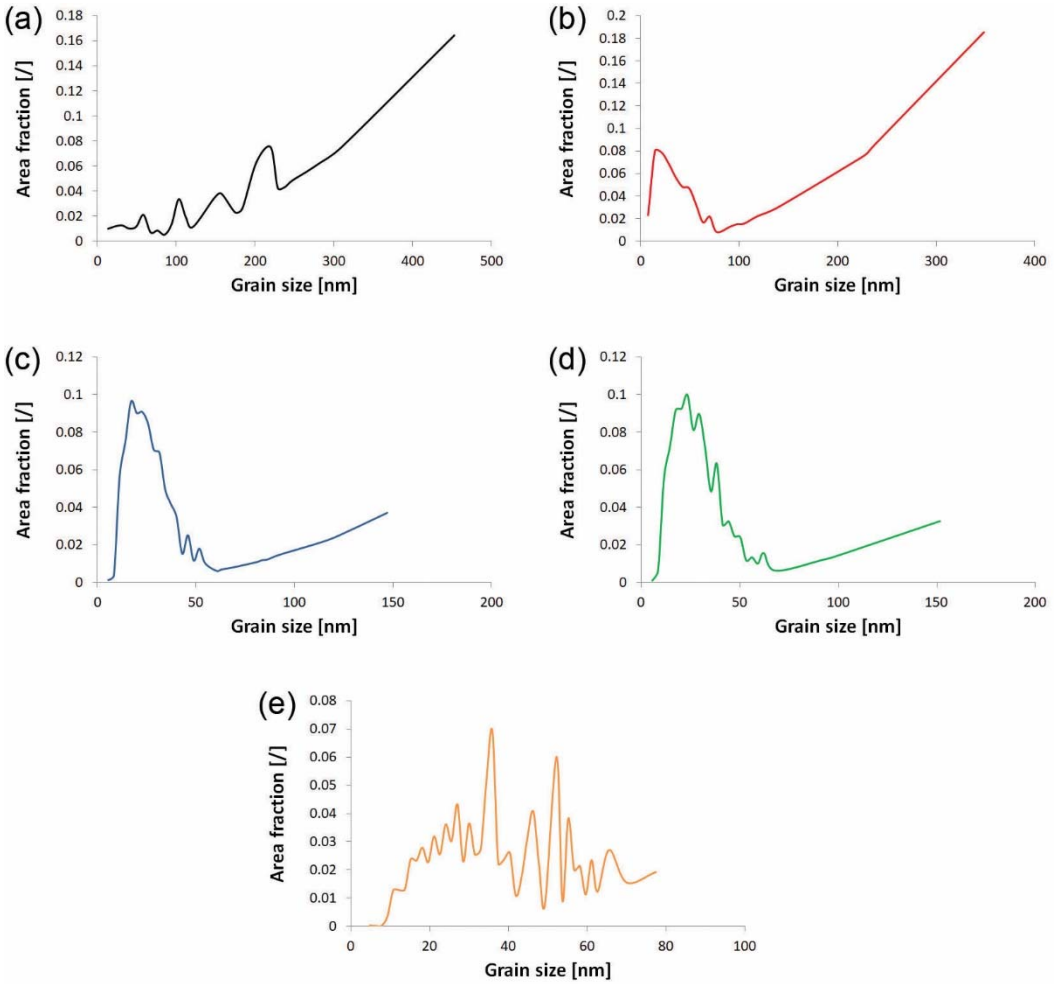

Figure 2: (a) Grain size distribution of the 0.27 Pa, (b) 0.40 Pa (c) 0.53 Pa (d) 0.67 Pa and (e) 1.07 Pa samples.

Pressure (Pa)	Average grain size (nm)	Mean stress (MPa/nm)
0.27	40 (10)	0.67 (9.62)
0.40	22 (24)	491 (17)
0.53	19 (3)	705 (10)
0.67	20 (4)	809 (10)
1.07	22 (3)	367 (18)

Table 2: Average grain size and mean stress per film. The numbers in between brackets represent the standard deviation.

It is worth noting that the films used in the present work have no strong (111) texture along the growth direction, although this is commonly expected in fcc thin films [31]. This was proven through (111) pole figures which show the texture parallel with the growth direction; these figures are provided in Figure 3. Generally, the (111) orientation along the growth direction is preferred in fcc metals due to the low interfacial energy of this plane [31]. The

expected texture can change because of, for example, impurities that can influence the interfacial energies, the nucleation sites and/or surface diffusivities [31]. Perpendicular to the growing direction, as shown in Figure 1b, it seems that at higher Ar pressure the films have a distinct {110} texture. This is also displayed in the inverse pole figures in Figure 4.

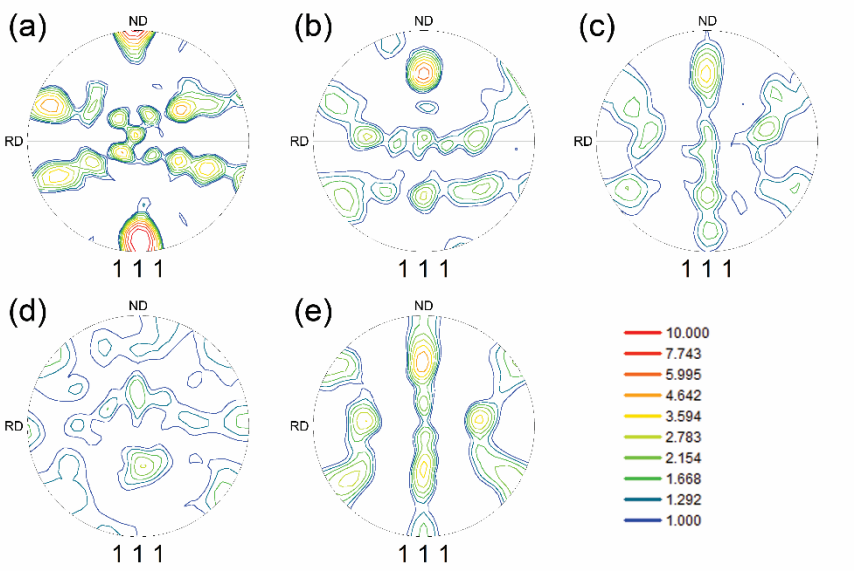

Figure 3: (a) (111) pole figure viewed parallel to the growth direction for the 0.27 Pa sample. (b) same for the 0.40 Pa (c) 0.53 Pa (d) 0.67 Pa and (e) 1.07 Pa samples. (ND = normal direction to the FIB; RD = rolling direction inside the film parallel to the substrate).

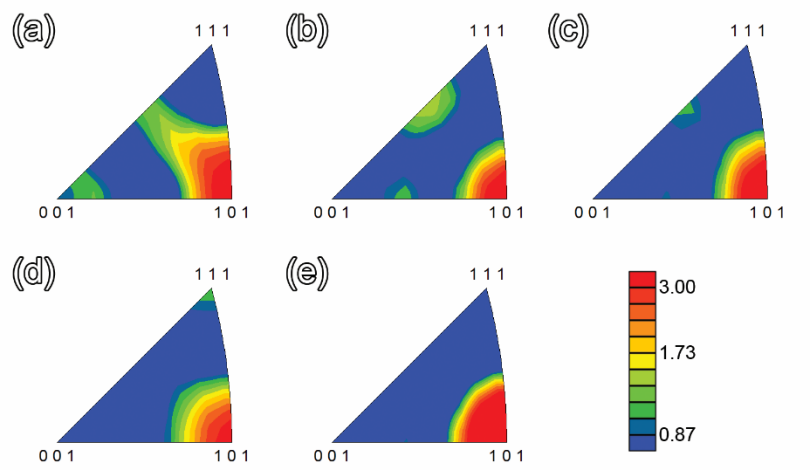

Figure 4: Inverse pole figures showing the distribution of texture in the FIB samples. (a) 0.27 Pa (b) 0.40 Pa (c) 0.53 Pa (d) 0.67 Pa and (e) 1.07 Pa.

So far, all TEM observations are consistent with the predictions from the stress-thickness data. The delay in stress-build up has been explained by the agglomeration of large grains on the substrate side, while the comparable increasing stress.thickness slope has been clarified by a similarity in grain size. Regarding the downwards bending slope, it was noticed that even though the samples deposited with 0.67 Pa and 1.07 Pa have a similar texture (Figure 1b) and grain size distribution (Figure 2), the curve of the downwards bending slope of the internal

stress is clearly stronger in the latter (Figure 1a). An explanation can be found using the GBs and Σ3 twin boundaries (TBs).

In this respect, Figure 5a shows the same maps as Figure 1b, but with the orientation colour overlay removed. Some of the present high angle GBs (HAGBs) are recognized as Σ3 TBs (blue lines in Figure 5). These are identified based on a misorientation plane of 60°±9° and a common plane between the neighbouring grains, which are the conditions according to the Brandon criteria for Σ3 {111} coincident site lattice boundaries [28, 29]. In this work, we show that Σ3 TBs are abundantly present in the films, even though Ni has a high stacking fault energy (~120-130 $mJ.m^{-2}$) [33]. This is not a unique phenomenon as growth twins were also observed in other materials with a high SFE such as in electron beam evaporated Pd thin films [34] and electrodeposited Al [35]. In the maps, some Σ3 boundaries appear to be curved which can due to the limitations from the ACOM-TEM or by the presence of Σ3 {112} ITBs. A TB density can be calculated per sample based on the total sum of the lengths of these Σ3 TBs divided by the total surface area of the accompanying sample; this is displayed in

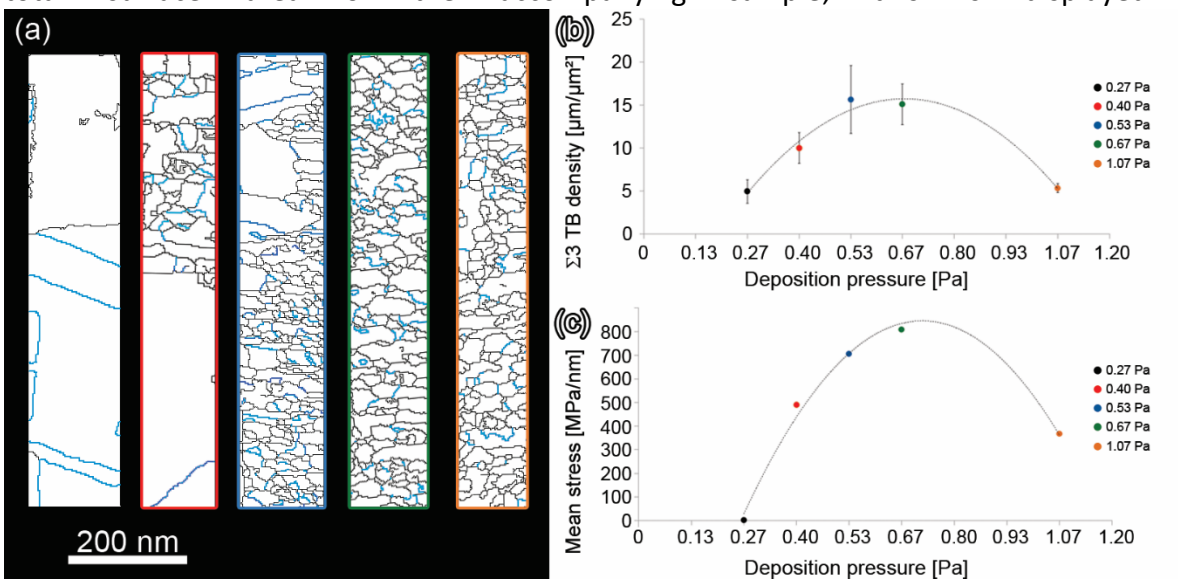

Figure **5**b. It shows that the 0.27, 0.40 and 1.07 Pa films have a relatively low TB density, while 0.53 and 0.67 Pa are comparably high.

Next, from Figure 1a, the mean internal stress per sample can be extracted from each curve (Figure 5c). This value is determined by dividing the final stress from the tail-end of that curve by the total deposition thickness. Cross-correlating this stress behaviour with the TB density shown in Figure 5b displays a clear connection. In the 0.27, 0.40, 0.53 and 0.67 Pa samples, the increase of the mean stress observed in Figure 5c is attributed to the increase of the density of GBs. When the internal elastic energy (IEE) reaches high levels such as in the 0.53 and 0.67 Pa samples, the local stress could reach values higher than the yield strength leading to the formation of dislocations. However, because of the high density of GBs and TBs in these samples, the internal stress cannot be relaxed since both GBs [36] and TBs [37–41] act as barriers for dislocation motion. Other mechanisms involving GB mediated processes could also play a role. In this case, twin boundaries, being more stable, could stabilize the grain structure and decrease the influence of grain boundary mediated stress relaxation. For the 1.07 Pa sample, however, the mean stress is significantly lower in comparison to the 0.67 Pa sample even though the HAGB density is similar. The difference can be found in the Σ3 TB density as shown in Figure 5b, implying that TBs have a significant influence on dislocation

motion. Indeed, because of the smaller density of TBs in the 1.07 Pa sample, dislocations can escape more easily leading to the relaxation of the internal stress. The low TB density in the 1.07 Pa sample can be attributed to the deposition rate used. Indeed, Amin-Ahmadi *et al*. observed a proportional correlation between the density of growth twins in nanocrystalline Pd thin films deposited with electron beam evaporation and the used deposition rate [16,34]. On the other hand, the average twin spacing and grain size remained approximately unchanged. Considering that in our work the deposition rate was decreased with increasing Ar pressure and that the average grain size remained consistent at higher pressure, we can conclude that only the twin boundary density will be affected, as shown in this study.

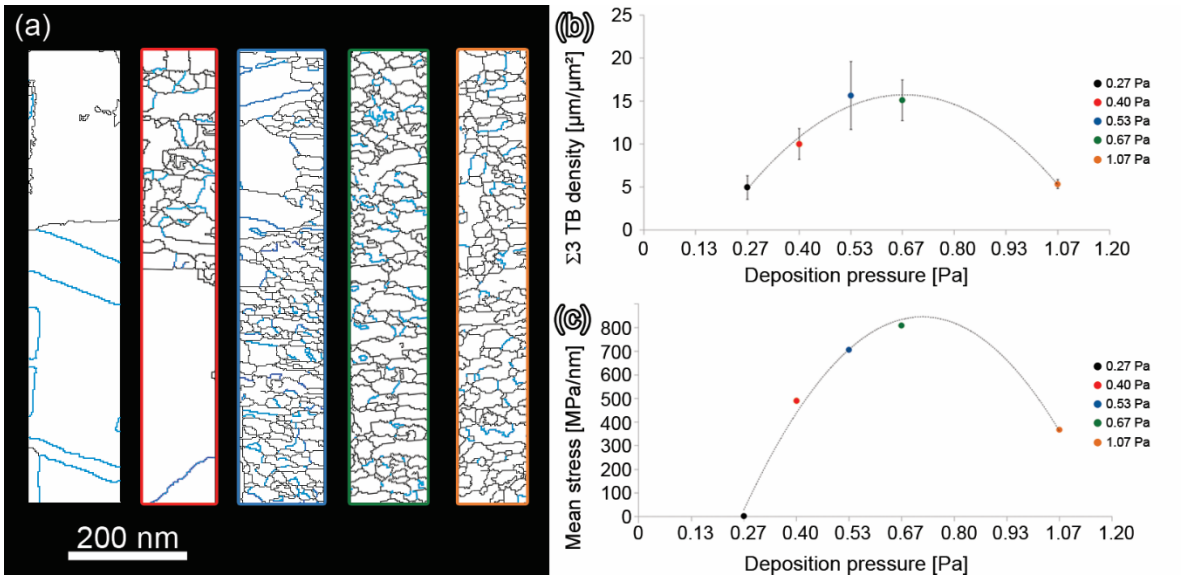

Figure 5: Blank ACOM-TEM maps highlighting the HAGBs. The Σ3 TBs are marked as blue lines. (b) Σ3 TB density as a function of deposition pressure. Error bars are added based on the Σ3 TB density spread from ACOM-TEM maps of different regions. (c) Mean internal stress as a function of deposition pressure, obtained from the stress-thickness curves of Figure 1a.

4. Conclusions

The origin of internal stress build-up in sputter-deposited Ni thin films was explained based on ACOM-TEM analysis. It was shown that there is a clear correlation between the thickness from which the internal stress starts building up and the presence of large grains close to the substrate in agreement with the 'nucleation layer' model. The similarity between the films in internal stress increase in the beginning of the growth is correlated with a comparable grain size, which is in accordance with the island coalescence model. The low internal stress at low Ar pressure is justified by the small amount of grain/twin boundaries, induced by the low amount of scattering during deposition. With increasing pressure, even though the deposition rate is adjusted, the scattering induces smaller grains which increase the internal stress of the film. At the highest Ar pressure, this effect is counterbalanced by a decreased Σ3 TB density due to the low deposition rate. This allows more relaxation of the internal stress by reducing the confinement of dislocations in grains in which local plasticity can be activated.

5. Acknowledgements

This work was supported by the Hercules Foundation [Grant No. AUHA13009], the Flemish Research Fund (FWO) [Grant No. G.0365.15N], and the Flemish Strategic Initiative for Materials (SIM) under the project InterPoCo. Thin film deposition has been realised as part of the WallonHY project, funded by the Public Service of Wallonia – Department of Energy and Sustainable Building. H. Idrissi is mandated by the Belgian National Fund for Scientific Research (FSR-FNRS).

6. References

[1] A. Oudriss, J. Creus, J. Bouhattate, C. Savall, B. Peraudeau, X. Feaugas, The diffusion and trapping of hydrogen along the grain boundaries in polycrystalline nickel, Scr. Mater. 66 (2012) 37–40. https://doi.org/10.1016/j.scriptamat.2011.09.036.

[2] X. Xu, M. Wen, Z. Hu, S. Fukuyama, K. Yokogawa, Atomistic process on hydrogen embrittlement of a single crystal of nickel by the embedded atom method, Comput. Mater. Sci. 23 (2002) 131–138. https://doi.org/10.1016/S0927-0256(01)00217-8.

[3] Z. Shan, E.A. Stach, J.M.K. Wiezorek, J.A. Knapp, D.M. Follstraedt, S.X. Mao, Grain Boundary – Mediated Plasticity in Nanocrystalline Nickel, Science (80-.). 305 (2004) 654–657.

[4] F.A. Doljack, R.W. Hoffman, The origins of stress in thin nickel films, Thin Solid Films. 12 (1972) 71–74. https://doi.org/10.1016/0040-6090(72)90396-3.

[5] C. Friesen, C. V. Thompson, Reversible Stress Relaxation during Precoalescence Interruptions of Volmer-Weber Thin Film Growth, Phys. Rev. Lett. 89 (2002) 1–4. https://doi.org/10.1103/PhysRevLett.89.126103.

[6] J. Rottler, D.J. Srolovitz, R. Car, Point defect dynamics in bcc metals, Phys. Rev. B - Condens. Matter Mater. Phys. 71 (2005) 1–12. https://doi.org/10.1103/PhysRevB.71.064109.

[7] L.B. Freund, S. Suresh, Thin Film Materials: Stress, Defect Formation and Surface Evolution, Cambridge University Press, Cambridge, 2003.

[8] S. Raghavan, X. Weng, E. Dickey, J.M. Redwing, Correlation of growth stress and structural evolution during metalorganic chemical vapor deposition of GaN on (111) Si, Appl. Phys. Lett. 88 (2006) 1–3. https://doi.org/10.1063/1.2168020.

[9] R.C. Cammarata, Surface and interface stress effects in thin films, Prog. Surf. Sci. 46 (1994) 1–38. https://doi.org/10.1016/0079-6816(94)90005-1.

[10] W.D. Nix, B.M. Clemens, Crystallite coalescence: A mechanism for intrinsic tensile stresses in thin films, J. Mater. Res. 14 (1999) 3467–3473.

[11] L.B. Freund, E. Chason, Model for stress generated upon contact of neighboring islands on the surface of a substrate, J. Appl. Phys. 89 (2001) 4866–4873. https://doi.org/10.1063/1.1359437.

[12] A. Godon, J. Creus, E. Conforto, F. Xavier, C. Savall, Effects of grain orientation on the Hall – Petch relationship in electrodeposited nickel with nanocrystalline grains, Scr. Mater. 62 (2010) 403–406. https://doi.org/10.1016/j.scriptamat.2009.11.038.

[13] J. Li, J.Y. Zhang, L. Jiang, P. Zhang, K. Wu, G. Liu, J. Sun, Twinning/detwinning-mediated grain growth and mechanical properties of free-standing nanotwinned Ni foils: Grain size and strain rate effects, Mater. Sci. Eng. A. 628 (2015) 62–74. https://doi.org/10.1016/j.msea.2015.01.015.

[14] B. Wang, H. Idrissi, M. Galceran, M.S. Colla, S. Turner, S. Hui, J.P. Raskin, T. Pardoen, S. Godet, D. Schryvers, Advanced TEM investigation of the plasticity mechanisms in nanocrystalline freestanding palladium films with nanoscale twins, Int. J. Plast. 37 (2012) 140–156. https://doi.org/10.1016/j.ijplas.2012.04.003.

[15] G. Lumbeeck, H. Idrissi, B. Amin-Ahmadi, A. Favache, R. Delmelle, V. Samaee, J. Proost, T. Pardoen, D. Schryvers, Effect of hydriding induced defects on the small-scale plasticity mechanisms in nanocrystalline palladium thin films, J. Appl. Phys. 124 (2018) 225105. https://doi.org/10.1063/1.5055274.

[16] B. Amin-Ahmadi, H. Idrissi, M. Galceran, M.S. Colla, J.P. Raskin, T. Pardoen, S. Godet,

D. Schryvers, Effect of deposition rate on the microstructure of electron beam evaporated nanocrystalline palladium thin films, Thin Solid Films. 539 (2013) 145–150. https://doi.org/10.1016/j.tsf.2013.05.083.
[17] J. Kacher, K. Hattar, I.M. Robertson, Initial texture effects on the thermal stability and grain growth behavior of nanocrystalline Ni thin films, Mater. Sci. Eng. A. 675 (2016) 110–119. https://doi.org/10.1016/j.msea.2016.08.045.
[18] J. Kacher, P. Elizaga, S.D. House, K. Hattar, M. Nowell, I.M. Robertson, Thermal stability of Ni/NiO multilayers, Mater. Sci. Eng. A. 568 (2013) 49–60. https://doi.org/10.1016/j.msea.2013.01.033.
[19] S. Zaefferer, A critical review of orientation microscopy in SEM and TEM, Cryst. Res. Technol. 46 (2011) 607–628. https://doi.org/10.1002/crat.201100125.
[20] A. Delvaux, G. Lumbeeck, H. Idrissi, J. Proost, Effect of microstructure on hydrogen absorption into Ni thin film electrodes during alkaline water electrolysis, Resubmitted after Rev. to Electrochim. Acta. (n.d.).
[21] B. Amin-Ahmadi, H. Idrissi, R. Delmelle, T. Pardoen, J. Proost, D. Schryvers, High resolution transmission electron microscopy characterization of fcc→9R transformation in nanocrystalline palladium films due to hydriding, Appl. Phys. Lett. 102 (2013) 071911. https://doi.org/10.1063/1.4793512.
[22] R. Tuyaerts, O. Poncelet, J.P. Raskin, J. Proost, Internal stress and opto-electronic properties of ZnO thin films deposited by reactive sputtering in various oxygen partial pressures, J. Appl. Phys. 122 (2017). https://doi.org/10.1063/1.4996453.
[23] E.F. Rauch, M. Véron, Automated crystal orientation and phase mapping in TEM, Mater. Charact. 98 (2014) 1–9. https://doi.org/10.1016/j.matchar.2014.08.010.
[24] A. Kobler, C. Kübel, Challenges in quantitative crystallographic characterization of 3D thin films by ACOM-TEM, Ultramicroscopy. 173 (2017) 84–94. https://doi.org/10.1016/j.ultramic.2016.07.007.
[25] S.I. Wright, Random thoughts on non-random misorientation distributions, Mater. Sci. Technol. 22 (2006) 1287–1296. https://doi.org/10.1179/174328406X130876.
[26] D. Christy, A. Watanabe, T. Egawa, Influence of strain induced by AlN nucleation layer on the electrical properties of AlGaN/GaN heterostructures on Si(111) substrate, AIP Adv. 4 (2014) 107104. https://doi.org/10.1063/1.4897338.
[27] S.J. Hearne, J.A. Floro, Mechanisms inducing compressive stress during electrodeposition of Ni, J. Appl. Phys. 97 (2005) 014901. https://doi.org/10.1063/1.1819972.
[28] O.E. Kongstein, U. Bertocci, G.R. Stafford, In Situ Stress Measurements during Copper Electrodeposition on (111)-Textured Au, J. Electrochem. Soc. 152 (2005) 116–123. https://doi.org/10.1149/1.1854093.
[29] M.A. Paesler, H. Fritzsche, Measurement of internal stress in thin films, Rev. Sci. Instrum. 45 (1974) 114–115. https://doi.org/10.1063/1.1686421.
[30] H. Natter, M. Schmelzer, R. Hempelmann, Nanocrystalline nickel and nickel-copper alloys: Synthesis, characterization, and thermal stability, J. Mater. Res. 13 (1998) 1186–1197.
[31] S. Suwas, R.K. Ray, Crystallographic Texture of Materials, 1st ed., Springer, London, 2014.
[32] D.G. Brandon, The structure of high-angle grain boundaries, Acta Metall. 14 (1966) 1479–1484.
[33] C.B. Carter, S.M. Holmes, The stacking-fault energy of nickel, Philos. Mag. 35 (1977)

1161–1171. https://doi.org/10.1080/14786437708232942.
[34] B. Wang, H. Idrissi, H. Shi, M.S. Colla, S. Michotte, J.P. Raskin, T. Pardoen, D. Schryvers, Texture-dependent twin formation in nanocrystalline thin Pd films, Scr. Mater. 66 (2012) 866–871. https://doi.org/10.1016/j.scriptamat.2012.01.038.
[35] L.D. Rafailović, C. Gammer, C. Ebner, C. Rentenberger, A.Z. Jovanović, I.A. Pašti, N. V. Skorodumova, H. Peter Karnthaler, High density of genuine growth twins in electrodeposited aluminum, Sci. Adv. 5 (2019) 1–8. https://doi.org/10.1126/sciadv.aax3894.
[36] H. Van Swygenhoven, Grain boundaries and dislocations, Science (80-.). 296 (2002) 66–67. https://doi.org/10.1126/science.1071040.
[37] J.W. Christian, S. Mahajan, Deformation twinning, Prog. Mater. Sci. 39 (1995) 1–157. https://doi.org/10.1016/0079-6425(94)00007-7.
[38] L. Lu, Y. Shen, X. Chen, L. Qian, K. Lu, Ultrahigh Strength and High Electrical Conductivity in Copper, Science (80-.). 304 (2004) 422–426. https://doi.org/10.1126/science.1092905.
[39] L. Lu, R. Schwaiger, Z.W. Shan, M. Dao, K. Lu, S. Suresh, Nano-sized twins induce high rate sensitivity of flow stress in pure copper, Acta Mater. 53 (2005) 2169–2179. https://doi.org/https://doi.org/10.1016/j.actamat.2005.01.031.
[40] X. Zhang, A. Misra, H. Wang, M. Nastasi, J.D. Embury, T.E. Mitchell, R.G. Hoagland, J.P. Hirth, Nanoscale-twirming-induced strengthening in austenitic stainless steel thin films, Appl. Phys. Lett. 84 (2004) 1096–1098. https://doi.org/10.1063/1.1647690.
[41] J. Nordström, R. Siriki, J. Moverare, G. Chai, Deformation Twinning Behavior in High Ni-Austenitic Materials Deformation Twinning Behavior in High Ni-Austenitic Materials, Mater. Sci. Forum. 941 (2018) 1561–1596. https://doi.org/10.4028/www.scientific.net/MSF.941.1591.

7. Supplementary information

7.1. Focuses ion beam preparation details

Since we are working with nanocrystalline films and to avoid complete amorphization, the thickness of the FIB foil is aimed to lie between 20-40 nm, which is for our case ideal to minimize the amount of overlapping grains. The starting thickness of the samples cut by FIB from the films is usually ~3 µm. During thinning, while the thickness is still higher than 100 nm, the FIB is operated at 30 kV and the current is decreased proportional to the remaining thickness (ranging from 0.79 nA to 0.08 nA). Below 100 nm, the voltage and current are first lowered to 8 kV and 66 pA, and final thinning is performed at 2 kV with 23 pA.

7.2. HR-TEM of the Si/TiO_2/Ni interface

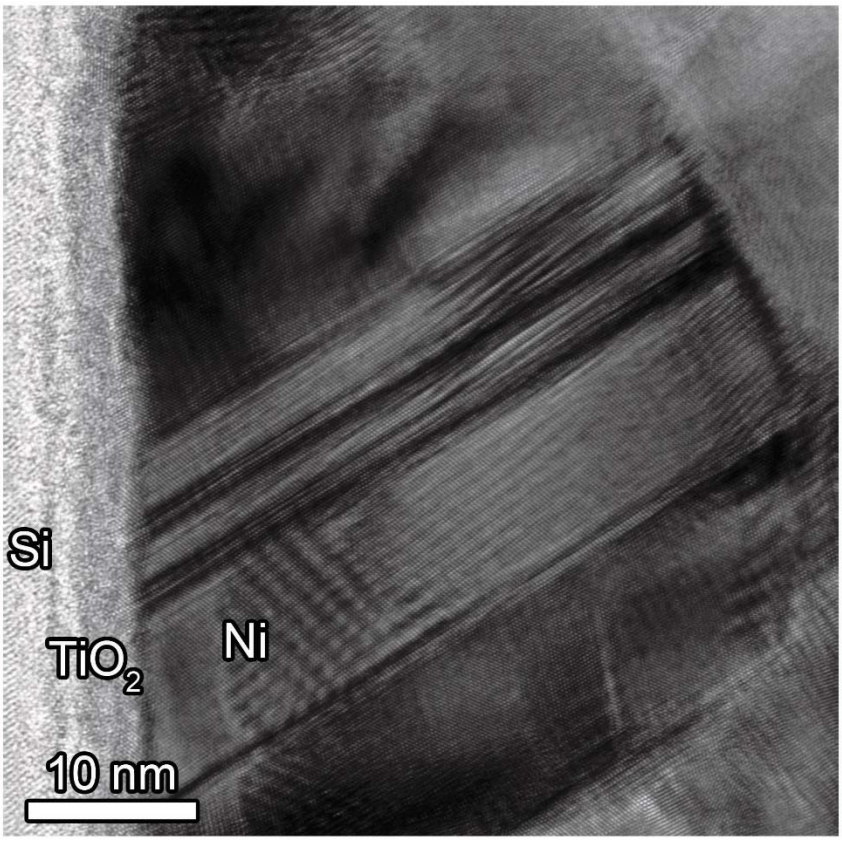

Figure S1: HR-TEM image showing the Si/TiO_2/Ni interface with the amorphous TiO_2 passivation layer.